Journal of Materials Chemistry A

Zeolitic Imidazolate Framework/Prussian Blue Analogue derived CoSe2/FeSe2 Heterostructure for Long-Cycle Aluminum-ion Battery

Journal:	*Journal of Materials Chemistry A*
Manuscript ID	TA-ART-11-2023-006734.R1
Article Type:	Paper
Date Submitted by the Author:	06-Jan-2024
Complete List of Authors:	Liu, Tianming; China University of Geosciences Beijing School of Science Liu, Meng; China University of Geosciences Beijing, School of Materials Science and Technology Guo, Juchen; University of California at Riverside, Chemical and Environmental Engineering Zhao, Changchun; China University of Geosciences, School of Science Liu, Hao; China University of Geosciences Beijing Li, Xiaowei; China University of Geosciences Beijing, School of Materials Science and Technology Liao, Libing; China University of Geosciences, Beijing, School of Materials Sciences and Technology Lv, Guocheng; China university of Geosciences,

Zeolitic Imidazolate Framework/Prussian Blue Analogue derived $CoSe_2/FeSe_2$ Heterostructure for Long-Cycle Aluminum-ion Battery

Tianming Liu [a], Meng Liu [b], Juchen Guo [c], Changchun Zhao [a, *], Hao Liu [a], Xiaowei Li [b], Libing Liao [b], Guocheng Lv [b, *]

[a] School of Science, China University of Geosciences, Beijing, 100083, China.

[b] Engineering Research Center of Ministry of Education for Geological Carbon Storage and Low Carbon Utilization of Resources, Beijing Key Laboratory of Materials Utilization of Nonmetallic Minerals and Solid Wastes, National Laboratory of Mineral Materials, School of Materials Science and Technology, China University of Geosciences (Beijing), 100083, China.

[c] Department of Chemical and Environmental Engineering, University of California, Riverside, California 92521, United States; Materials Science and Engineering Program, University of California, Riverside, California 92521, United States.

* Corresponding authors.

E-mail addresses: zhaocc@cugb.edu.cn (C. Zhao), guochenglv@cugb.edu.cn (G. Lv)

Keywords

Aluminum-ion battery, Heterostructure, MOF, $CoSe_2/FeSe_2$, Density functional theory

Abstract

Aluminum-ion batteries (AIBs) have been considered a low-cost, safe and high energy density candidate for large-scale electrochemical energy storage system. Here, we utilize the concept of interface engineering to synthesize a $CoSe_2/FeSe_2$ heterostructure cathode through MOF-on-MOF heteroepitaxial growth. The presence of an internal electric field between the $CoSe_2$ and $FeSe_2$ phases induces a synergistic effect to achieve rapid charge transfer and ion diffusion, which enables facile conversion reaction based on Co^{2+}/Co^0 and Fe^{2+}/Fe^0. The $CoSe_2/FeSe_2$ heterostructure displays an initial discharge capacity of 356.9 mAh g^{-1} at 100 mA g^{-1}. After 1600 cycles at 200 mA g^{-1}, the reversible capacity is 133.7 mA g^{-1}. Theoretical calculation also demonstrates that the designed $CoSe_2/FeSe_2$ heterostructure can significantly

promote the directional electron transfer and reduce the aluminum-ions migration barrier energy. Therefore, the concept of heterostructure cathodes provides a strategy to develop long-cycle life AIBs.

1. Introduction

With the great demand of clean energy for social progress, the development of aluminum ion battery (AIB) system has attracted increasing attention [1-9]. Aluminum anode has the superiority of excellent theoretical volumetric capacity (8046 mAh cm^{-3}), crustal content abundance (8.2 wt.%), and high safety factor [10-15]. AIBs are likely to be a replacement for lithium-ion batteries in applications such as large-scale grid energy storage, electric transportation, and electricity supply [16-20]. However, the large size of chloroaluminate anions of the electrolyte and the high charge density of aluminum ions limit the fast reaction kinetics of aluminum-ion batteries and hinder their practical applications [21-25].

Among the conversion-type cathode materials for AIBs, transition metal chalcogenides such as FeS_2 [26, 27], $CoSe_2$ [28-31] and NiTe [32] have the advantages of high capacity and electronic conductivity. However, the key factors that seriously affect battery performance are the slow diffusion of aluminum ions and the pulverization of the material structure during cycling. [33-38]. Therefore, the rational design of electrode materials is key in improvement of cycle life and energy density of AIBs. As previously reported, Bi_2Te_3/Sb_2Te_3 [39], $ZnSe/SnSe_2$ [40], $FeSe_2/MoS_2$ [41] and $Co_3Se_4/ZnSe$ [42] heterostructure materials have internal electric fields between the interfaces, enabling fast charge transfer and ion diffusion [43-49]. Cathode materials can provide excellent performance for AIBs based on the conversion mechanism, but only the active material of one phase provides charge transfer and the other phase usually provides physical support to prevent the collapse during the cycle. Consequently, the construction of heterostructure active materials is crucially to accelerate the comprehensive performance of AIBs.

Here, we present a new strategy to design transition metal selenide heterostructure materials. The core-shell structure of ZIF-67/Co-Fe PBA was synthesized based on the

MOF-on-MOF heteroepitaxial growth strategy and the hollow $CoSe_2/FeSe_2$ nanocubes heterostructure were obtained from one-step annealing. The presence of an internal electric fields at the heterostructure interface can facilitate the reaction kinetics of the reversible redox reactions of Co^{2+}/Co^0 and Fe^{2+}/Fe^0 and provide excellent capacity performance. Additionally, the unique hollow nanostructure can alleviate the volume expansion, resulting in ultra-long cycle life. The $CoSe_2/FeSe_2$ heterostructure demonstrated excellent AIBs capability, maintaining a reversible capacity of 133.7 mA g^{-1} after 1600 cycles at 200 mA g^{-1}.

2. Results and discussion

The scanning electron microscopy (SEM), transmission electron microscopy (TEM), and element mapping were used to characterize the microstructure and composition of $CoSe_2/FeSe_2$ heterostructure. We first synthesized ZIF-67 nanocubes as a precursor (**Fig. 1a**), and prepared core-shell ZIF-67/Co-Fe PBA nanocubes with the anion exchange method. **Fig. 1b, d** and **Fig. S1** shown the uniform distribution of ZIF-67/Co-Fe PBA, and the element mapping indicated that $[Fe(CN)_6]^{3-}$ was successfully exchanged into core-shell structure [50-54]. Subsequently, ZIF-67/Co-Fe PBA core-shell nanocubes were uniformly mixed with selenium powder and converted to $CoSe_2/FeSe_2$ by annealing in argon atmosphere. After selenization, the hollow structure was formed due to the different metal diffusion rate of Kirkendall effect [55-57], and $CoSe_2/FeSe_2$ nanoparticles are evenly distributed within carbon nanocubes (**Fig. 1c** and **1e**). The heterostructure boundary of $CoSe_2$ and $FeSe_2$ nanoparticles is clearly seen in the high-resolution transmission electron microscopic (HRTEM) image in **Fig. 1f**, which are 2.533 Å at (111) plane of $CoSe_2$ and 2.397 Å at (200) plane of $FeSe_2$. In addition, elemental mapping indicated that Co, Fe and Se were evenly distributed throughout the hollow structure (**Fig. 1 g-i**). The thermogravimetric analysis (TGA) indicates that the carbon content of $CoSe_2/FeSe_2$ is approximately 26.79 wt.% (**Fig. S2**).

The crystal composition of $CoSe_2/FeSe_2$ heterostructure was determined from the X-ray diffraction (XRD) patterns in **Fig. 2a**, where the observed diffraction peaks of the orthorhombic $CoSe_2$ (JCPDS: 12-291) and orthorhombic $FeSe_2$ (JCPDS: 53-449)

almost completely overlapped. X-ray photoelectron spectroscopy (XPS) was employed to evaluate the chemical information of $CoSe_2/FeSe_2$ heterostructure. The Co 2p spectrum in **Fig. 2b** displays Co $2p_{1/2}$ peaks at 797.90 eV and 793.46 eV and Co $2p_{3/2}$ peaks at 779.03 eV and 778.19 eV, which proves the existence of Co^{2+} on the surface of $CoSe_2/FeSe_2$ heterostructure. The Fe 2p spectrum in **Fig. 2c** exhibits Fe $2p_{1/2}$ and Fe $2p_{3/2}$ of the Fe^{3+} state located at 723.59 eV and 713.29 eV and $2p_{1/2}$ and $2p_{3/2}$ of the Fe^{2+} state at 719.56 eV and 710.60 eV, respectively. Therefore, the original valence state of Fe in the $CoSe_2/FeSe_2$ heterostructure is Fe^{2+} and Fe^{3+}. The Se 3d spectrum in **Fig. 2d** shows the Se $3d_{3/2}$ peak at 55.68 eV and Se $3d_{5/2}$ peak at 54.78 eV, which are consistent with the Se_2^{2-} diselenide anion.

The electrochemical properties of the $CoSe_2/FeSe_2$ heterostructure are evaluated in the Swagelok cells with Al as the counter electrode. As a comparison, single-phase $CoSe_2$ particles were prepared using ZIF-67 as the precursor. The characterizations of $CoSe_2$ including TGA, XRD, SEM, TEM, and surface area analysis are in **Fig. S2** to **S6**. The galvanostatic charge and discharge (GCD) curves of the $CoSe_2/FeSe_2$ heterostructure in the first three cycles at a current density of 100 mA g^{-1} are shown in **Fig. 3a**. The first discharge and charge capacities of the $CoSe_2/FeSe_2$ heterostructure are 356.9 mAh g^{-1} and 438.6 mAh g^{-1}, thus the initial coulombic efficiency (CE) is 81.4%. The excess charge capacity may be due to the electro-oxidation of the Se_2^{2-} anion, which is evidenced by the Se 3d XPS spectra after discharge and charge displayed in **Fig. 4c**. The single-phase $CoSe_2$ only exhibits 241.5 mAh g^{-1} discharge capacity and 393.4 mAh g^{-1} charge capacity in the first cycle with a 61.4% initial CE (**Fig. S7**). **Fig. 3b** compares the cyclic stability between the $CoSe_2/FeSe_2$ heterostructure and the single-phase $CoSe_2$, after 100 cycles the discharge capacity of $CoSe_2/FeSe_2$ cathode remains at 162.5 mAh g^{-1}, which almost two times higher than the 82.5 mAh g^{-1} of $CoSe_2$. The $CoSe_2/FeSe_2$ heterostructure also demonstrates very good rate performance as shown in **Fig. 3c**. it is also noticeable that the CE increases when the current density increases from 100 to 500 mA g^{-1}. The improved CE can be attributed to the kinetic limitation on the electro-oxidation of Se_2^{2-} due to enhanced charging overpotential. Long-cycle performance of the $CoSe_2/FeSe_2$ heterostructure

was tested at 200 mA g^{-1} (**Fig. 3d)**. The initial capacity of $CoSe_2/FeSe_2$ is 243.1 mAh g^{-1}, which can be maintained at 133.7 mAh g^{-1} after 1600 cycles. A stable coulombic efficiency of 92% proves superior long-term operational durability, benefit to the hollow structure of $CoSe_2/FeSe_2$ heterostructure, the volume expansion during the long-cycle can be efficiently alleviated. Electrochemical properties of $CoSe_2/FeSe_2$ cathode material and some representative transition metal chalcogenides and heterostructures are displayed in **Table S1**. The $CoSe_2/FeSe_2$ heterostructure has outstanding cycle life and capacity performance, as well as the best ultra-long recyclability of selenide heterojunction cathode materials reported to date. The cyclic voltammetry (CV) curves of the $CoSe_2/FeSe_2$ heterostructure at different scan rate (1, 2, 3, 4, and 5 mV s^{-1}) are shown in **Fig. 3e**. The peak current (i) and scan rate (v) can be corelated by the equation of $i = \alpha v^b$. [58] When the b-value = 0.5, the process can be considered a semi-infinite diffusion control process of ions in the electrode material (such as typical intercalation-type martials); b-value = 1 indicates a surface-redox controlled process determined by the intrinsic reaction rate. The b-values of the oxidation and reduction of $CoSe_2/FeSe_2$ were 0.844 and 0.856, respectively, shown in **Fig. 3f**. On the other hand, the b-values of the oxidation and reduction of the single-phase $CoSe_2$ were 0.707 and 0.714 (**Fig. S8**). It is clear that the b-value of the heterostructure increased significantly, indicating that the heterostructure facilitates the reaction kinetics of electrochemical redox.

To shed some light on the mechanism of the electrochemical reaction of the $CoSe_2/FeSe_2$ heterostructure cathode and aluminum-ion, the cathodes were characterized with XPS after the first full discharge and the first full charge. According to **Fig. 4a,** the fully discharged Co 2p spectra show that the peak intensity of Co^{2+} decreases and Co^0 peak appears at 778.59 eV, indicating that Co^{2+} is reduced to Co^0 during discharge. The spectrum of fully charged Co 2p shows the peak of 781.90eV is Co^{2+}. The XPS spectra of Fe 2p after electrochemical reaction are shown in **Fig. 4b**. After full discharge, the XPS Fe 2p spectra can be distinguished as Fe^0 peaks located at 707.45 eV and 719.18 eV and Fe^{2+} peaks located at 710.49 eV and 723.15 eV. The Fe^{3+} peaks observed in the pristine $CoSe_2/FeSe_2$ heterostructure (**Fig. 2c**) completely disappear, indicating reduction of Fe^{3+}. After charging, only Fe^{2+} peaks at 710.17 eV

and 723.29 eV were detected, indicating the redox reaction of iron is between Fe^{2+} and Fe^0 by two-electron transfer, and the reduction of Fe^{3+} only occurs in the first discharge. This suggests that the electrochemical reaction process involves the redox reaction of Co^{2+}/Co^0 and Fe^{2+}/Fe^0. **Fig. 4c** reveals the Se 3d spectra after the first discharge and charge. The binding energy of the Se 3d XPS peaks after discharge is consistent with that of the pristine $CoSe_2/FeSe_2$ heterostructure (**Fig. 2d**). After charging, the binding energy of Se 3d becomes higher, indicating possible oxidation of the Se_2^{2-} anion, which may explain the excess charge capacity of $CoSe_2/FeSe_2$ (**Fig. 3a**). Moreover, the content of Al increases after discharge, while the peak intensity of Al decreases with the electrochemical desorption after charging (**Fig. 4d**). The structure composition of the $CoSe_2/FeSe_2$ electrodes after 200 cycles were characterized with the HRTEM as displayed in **Fig. S9**. The $CoSe_2/FeSe_2$ electrode still maintains nanostructure after cycling. The lattice fringes detected after full discharge are Co^0 (2.185 Å) and Fe^0 (2.063 Å); and the lattice fringes of $CoSe_2$ (2.903 Å) and $FeSe_2$ (3.022 Å) were detected after charging, which are consistent with the XPS results.

According to the above results, the possible discharge-charge reactions of the $CoSe_2/FeSe_2$ cathode are proposed as follows:

$$CoSe_2 + 2/3Al^{3+} + 2e^- \leftrightarrow Al_{2/3}Se_2 + Co \quad (1)$$

$$FeSe_2 + 2/3Al^{3+} + 2e^- \leftrightarrow Al_{2/3}Se_2 + Fe \quad (2)$$

The heterostructure properties of $CoSe_2/FeSe_2$ interface are studied with computational methods based on density functional theory (DFT). As displayed in **Fig. 5a**, the density of states (DOS) of $CoSe_2/FeSe_2$ heterostructure near Fermi level is enhanced than $CoSe_2$ and $FeSe_2$, which means that the introduction of interface engineering leads to an enhanced conductivity. **Fig. 5b** shows the work function curves of the $CoSe_2$, $FeSe_2$ and $CoSe_2/FeSe_2$ heterostructure. The $CoSe_2$ has a work function of 4.951 eV, which is lower than $FeSe_2$ (5.015 eV). This indicates that the internal electric field leads to directed electron transport, demonstrating the path from $CoSe_2$ to $FeSe_2$. In the conventional P-N heterojunction, the transport of electrons and holes proceeds in opposite directions until equilibrium is reached at the Fermi level. $FeSe_2$[59,

[60] and $CoSe_2$[61, 62] are typical p-type and n-type semiconductors, the internal electric field and electron flow direction constructed by the heterostructure interface was shown in **Fig. 5c**. The $CoSe_2$ and $FeSe_2$ of orthorhombic system have similar cell parameters, and the two surface lattices are well matched, resulting in a strong interaction at the interface. In **Fig. 5d**, the charge density contour plot in the plane proves the charge transfer and different distribution between interfaces. As shown in **Fig. 5e** and **Fig. S10**, the transition state search method was used to calculate the migration path and barrier energy of aluminum-ions on selenides. The $CoSe_2/FeSe_2$ heterostructure has a lower barrier of 0.26 eV compared to $CoSe_2$ (0.30 eV) and $FeSe_2$ (0.39 eV), indicating that the diffusion energy barrier of Al-ions can be reduced at the heterostructure interface and the reaction kinetics of AIBs can be accelerated. In **Fig. 5f,** the adsorption energy and electron difference density were calculated for the stable site of Al-ion at the electrodes interface. In comparison, the $CoSe_2/FeSe_2$ heterostructure has a greater adsorption energy (-1.41 eV) for aluminum-ions, indicating the structure is more stable during adsorption. During repeated electrochemical reactions, a more stable long-term performance may be achieved. As shown in **Fig. S11**, the electron density difference indicates an increase in charge transfer at the heterostructure interface, which enhances the charge transfer behavior and further improves the electrochemical performance. In conclusion, the DFT calculation further revealed the reason why $CoSe_2/FeSe_2$ heterostructure facilitate the reaction kinetics of Al-ion batteries.

3. Conclusion

In summary, based on the reasonable design of MOF-on-MOF, a hollow $CoSe_2/FeSe_2$ heterostructure was derived as the cathode of aluminum-ion batteries. Through heterogeneous interface engineering, the electrochemical kinetics of the conversion reaction has been greatly enhanced, and a favorable synergistic effect has been verified theoretically and experimentally. Therefore, the designed active electrode material is obviously strengthened, showing an ultra-long cycle life and excellent rate performance. Within the aluminum-ion battery system, the initial discharge capacity of $CoSe_2/FeSe_2$ electrode at 100 mA g^{-1} is 356.9 mAh g^{-1}. Even after 1600 cycles at 200

mA g^{-1}, the reversible capacity remains at 133.7 mAh g^{-1}. In view of our innovative strategy, the constructed heterojunction interface is expected to be developed in the electrochemical energy storage materials with long cycle life, providing significant reference value for aluminum-ion batteries.

Acknowledgements

This work was supported by the National Natural Science Foundation of China (No. 21875223). J. G. acknowledge the support from U.S. National Science Foundation through grant CBET-1751929.

Conflict of Interest

The authors declare no conflict of interest.

Supporting Information

Experimental section, characterization, electrochemical measurements, DFT calculations and other detailed results are included. Supporting information can be found online.

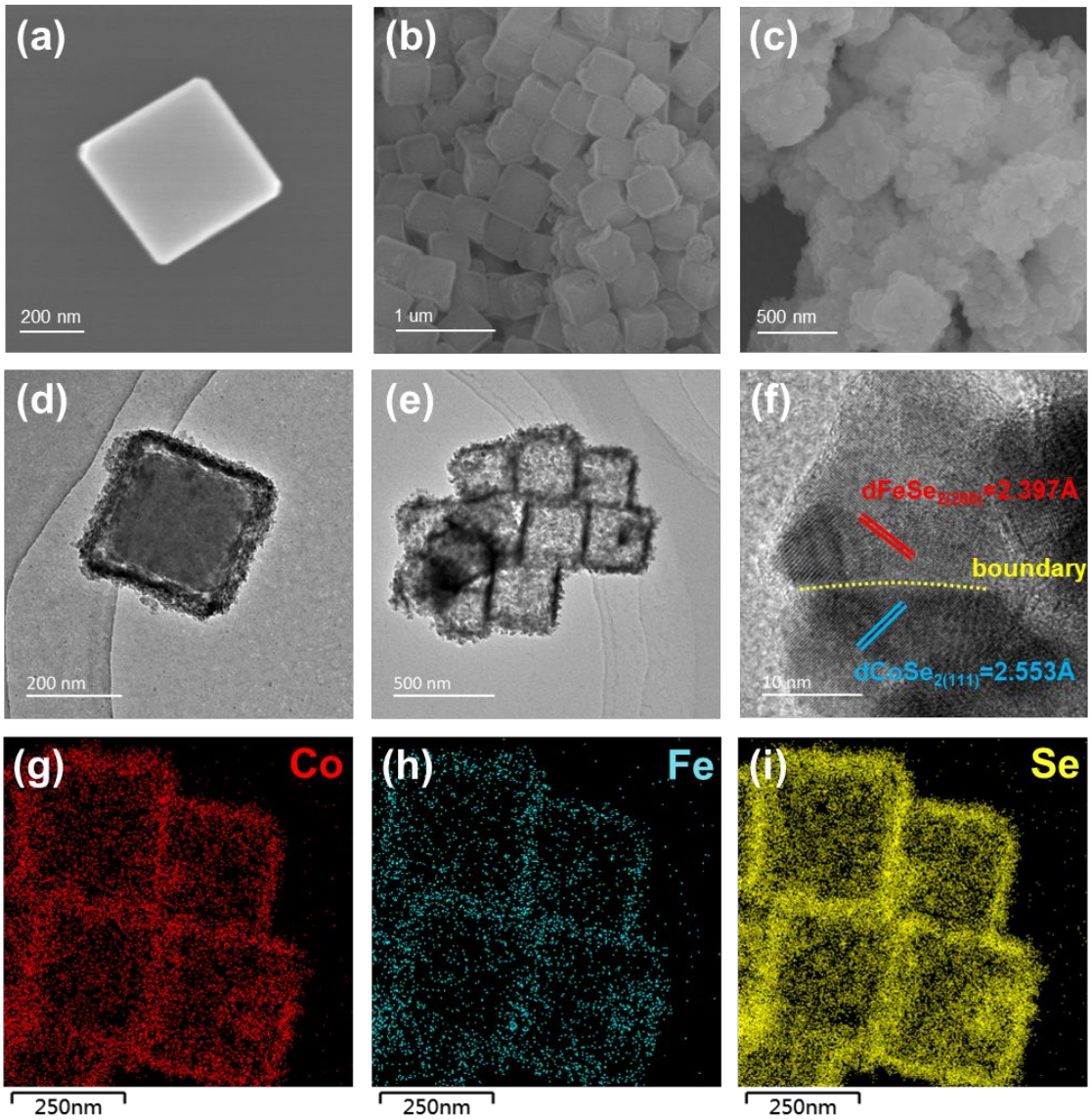

Fig. 1 Morphological and structural characterization. (a) SEM image of ZIF-67, SEM and TEM images of (b, d) ZIF-67/Co-Fe PBA and (c, e) $CoSe_2/FeSe_2$ heterostructure; (f-i) HRTEM and element mapping (Co, Fe and Se) of $CoSe_2/FeSe_2$ heterostructure.

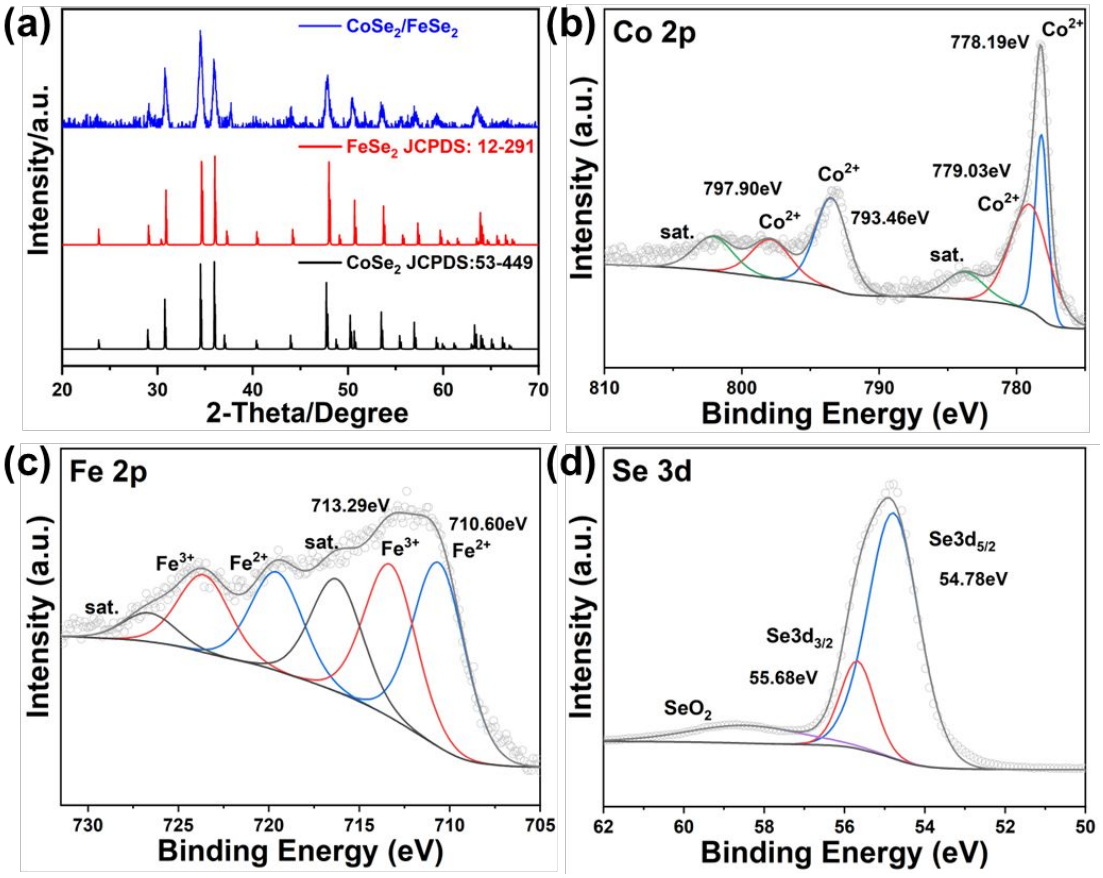

Fig. 2 Structural and chemical information. (a) XRD patterns of $CoSe_2/FeSe_2$ heterostructure. The XPS spectrum for $CoSe_2/FeSe_2$ heterostructure of (b) Co 2p, (c) Fe 2p and (d) Se 3d.

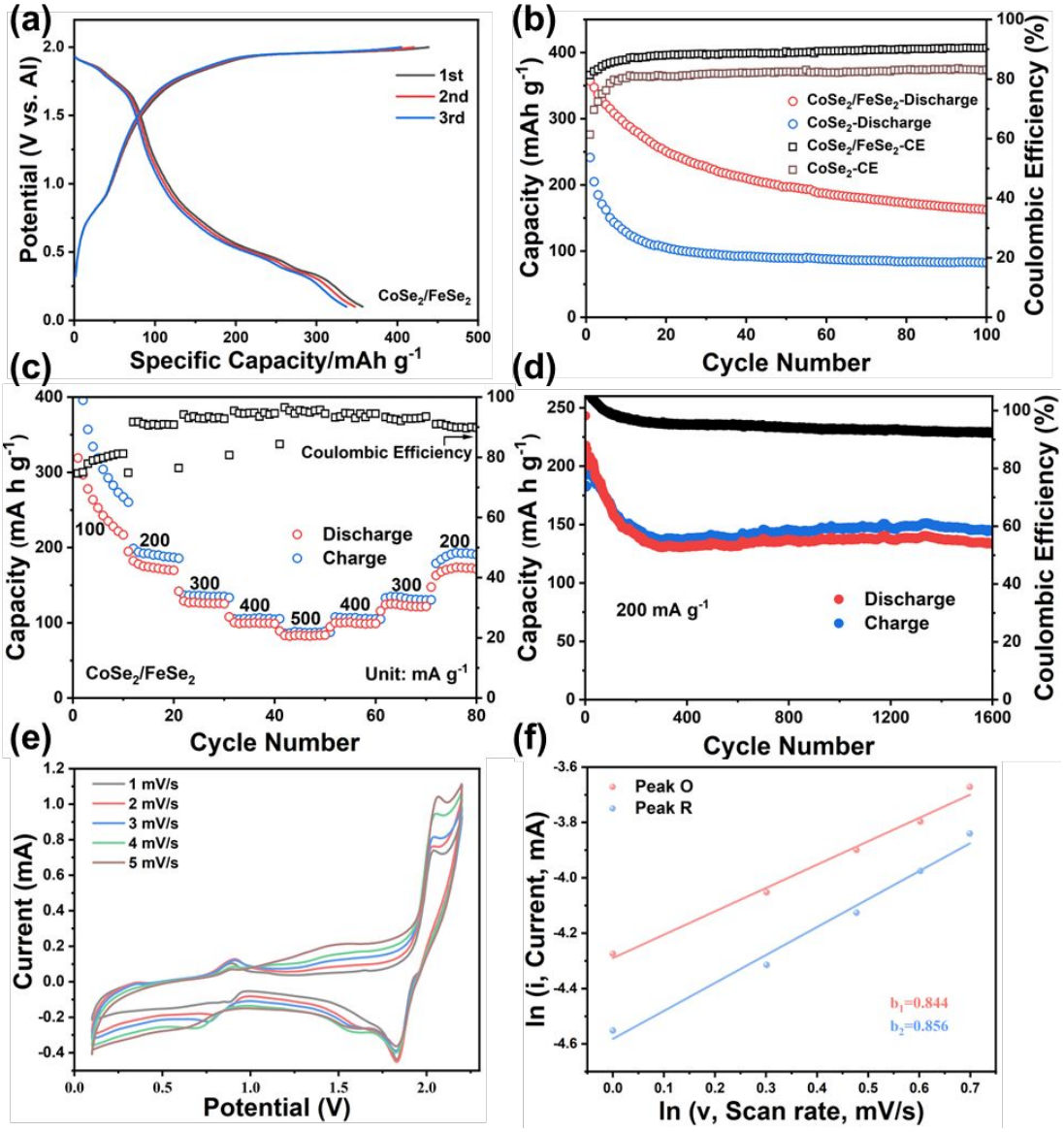

Fig. 3 Electrochemical performances. (a) The first three cycles of the $CoSe_2/FeSe_2$ heterostructure at a current density of 100 mA g^{-1}. (b) The cycle stability comparison between the $CoSe_2/FeSe_2$ heterostructure and the single-phase $CoSe_2$ at 100 mA g^{-1}. (c) Rate performance of the $CoSe_2/FeSe_2$ heterostructure from 100 to 500 mA g^{-1}. (d) Ultra-long cycle stability and CE of the $CoSe_2/FeSe_2$ heterostructure at 200 mA g^{-1}. (e) The CV curves of the $CoSe_2/FeSe_2$ heterostructure at different scan rate, and (f) the corresponding ln(i) vs. ln(v) plots.

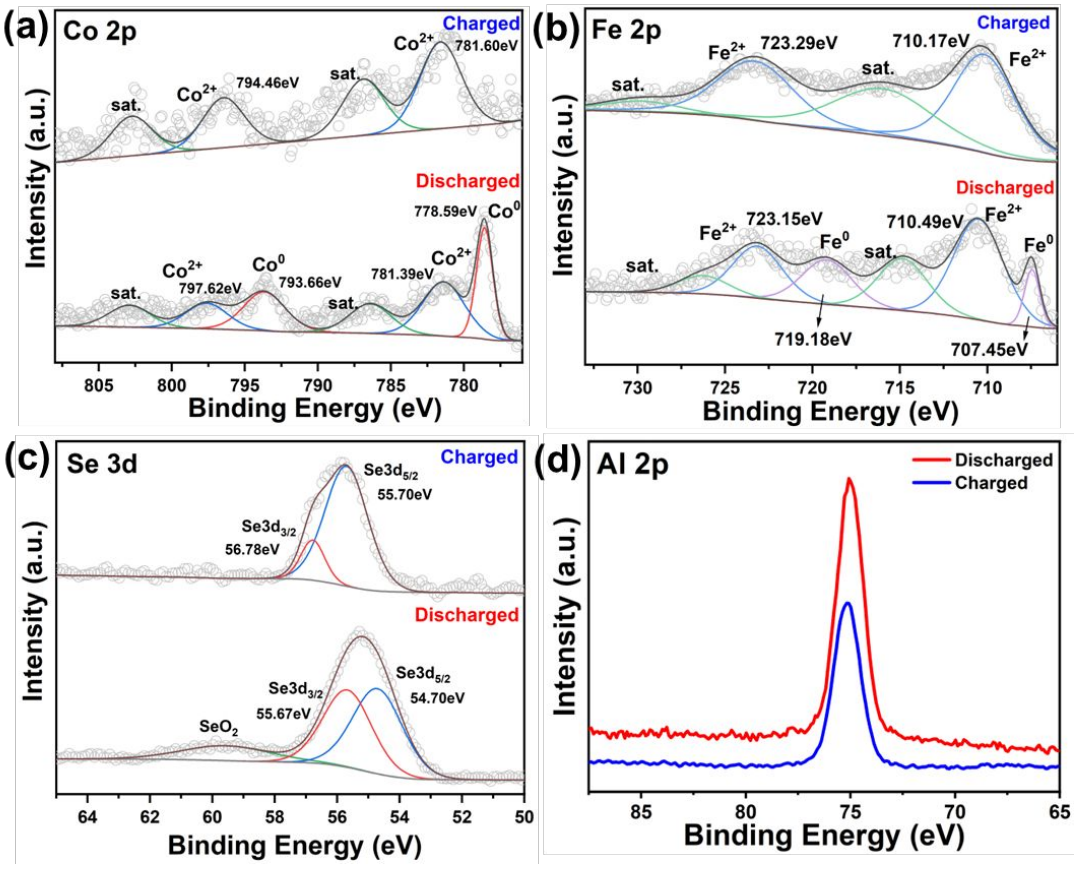

Fig. 4 Chemical information after the 1st cycle. The XPS spectrum of $CoSe_2/FeSe_2$ cathodes fully charged/discharged: (a) Co 2p, (b) Fe 2p, (c) Se 3d and (d) Al 2p.

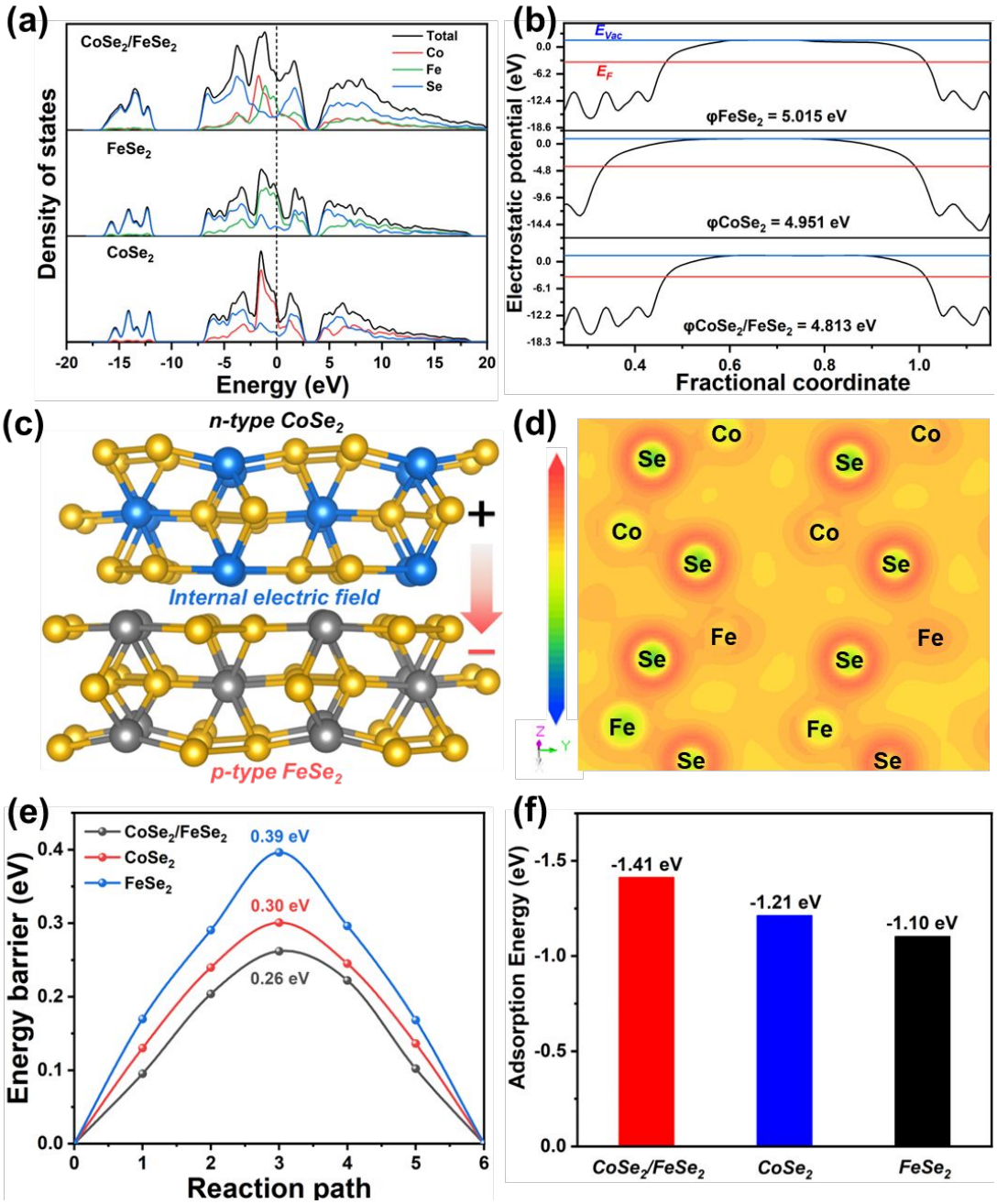

Fig. 5 DFT calculations. (a) DOS for $CoSe_2/FeSe_2$ heterostructure, $FeSe_2$ and $CoSe_2$. (b) The work function curves of $CoSe_2/FeSe_2$ heterostructure, $FeSe_2$ and $CoSe_2$. (c) Schematic for internal electric field and electron transfer of $CoSe_2/FeSe_2$ heterostructure. (d) Contour plot of charge density in a plane of $CoSe_2/FeSe_2$ heterostructure. The yellow and blue areas represent charge accumulation and consumption, respectively. (e) The barrier energy of $CoSe_2/FeSe_2$ heterostructure, $CoSe_2$ and $FeSe_2$. (f) The adsorption energy of aluminum-ions at the interface of $CoSe_2/FeSe_2$ heterostructure, $CoSe_2$ and $FeSe_2$.

Reference

1. Y. Kong, A. K. Nanjundan, Y. Liu, H. Song, X. Huang and C. Yu, *Small*, 2019, **15**, 1904310.
2. D. Munoz-Torrero, J. Palma, R. Marcilla and E. Ventosa, *Dalton Trans*, 2019, **48**, 9906-9911.
3. G. A. Elia, K. Marquardt, K. Hoeppner, S. Fantini, R. Lin, E. Knipping, W. Peters, J. F. Drillet, S. Passerini and R. Hahn, *Adv Mater*, 2016, **28**, 7564-7579.
4. S. Lee and J. Cho, *Angew Chem Int Ed Engl*, 2015, **54**, 9452-9455.
5. M. Li, J. Lu, X. Ji, Y. Li, Y. Shao, Z. Chen, C. Zhong and K. Amine, *Nature Reviews Materials*, 2020, **5**, 276-294.
6. A. Childress, P. Parajuli, S. Eyley, W. Thielemans, R. Podila and A. M. Rao, *Chemical Physics Letters*, 2019, **733**.
7. X. Yu, B. Wang, D. Gong, Z. Xu and B. Lu, *Adv Mater*, 2017, **29**.
8. S. K. Das, *Angew Chem Int Ed Engl*, 2018, **57**, 16606-16617.
9. N. Jayaprakash, S. K. Das and L. A. Archer, *Chemical Communications*, 2011, **47**, 12610-12612.
10. K. L. Ng, B. Amrithraj and G. Azimi, *Joule*, 2022, **6**, 134-170.
11. J. Tu, W.-L. Song, H. Lei, Z. Yu, L.-L. Chen, M. Wang and S. Jiao, *Chemical Reviews*, 2021, **121**, 4903-4961.
12. H. Xu, T. Bai, H. Chen, F. Guo, J. Xi, T. Huang, S. Cai, X. Chu, J. Ling, W. Gao, Z. Xu and C. Gao, *Energy Storage Materials*, 2019, **17**, 38-45.
13. H. Yang, H. Li, J. Li, Z. Sun, K. He, H. M. Cheng and F. Li, *Angew Chem Int Ed Engl*, 2019, **58**, 11978-11996.
14. P. Canepa, G. Sai Gautam, D. C. Hannah, R. Malik, M. Liu, K. G. Gallagher, K. A. Persson and G. Ceder, *Chem Rev*, 2017, **117**, 4287-4341.
15. M. Liu, G. Lv, H. Liu, Y. Fu, J. Zhang, L. Liao, D.-e. Jiang and J. Guo, *Advanced Functional Materials*, 2023, 2301913.
16. T. Gao, X. Li, X. Wang, J. Hu, F. Han, X. Fan, L. Suo, A. J. Pearse, S. B. Lee, G. W. Rubloff, K. J. Gaskell, M. Noked and C. Wang, *Angew Chem Int Ed Engl*, 2016, **55**, 9898-9901.
17. S. Liu, X. Zhang, S. He, Y. Tang, J. Wang, B. Wang, S. Zhao, H. Su, Y. Ren, L. Zhang, J. Huang, H. Yu and K. Amine, *Nano Energy*, 2019, **66**.
18. H. Li, H. Yang, Z. Sun, Y. Shi, H.-M. Cheng and F. Li, *Nano Energy*, 2019, **56**, 100-108.
19. Z. Lin, M. Mao, C. Yang, Y. Tong, Q. Li, J. Yue, G. Yang, Q. Zhang, L. Hong and X. Yu, *Science Advances*, 2021, **7**, eabg6314.
20. T. Liu, G. Lv, M. Liu, C. Zhao, L. Liao, H. Liu, J. Shi, J. Zhang and J. Guo, *Materials Chemistry Frontiers*, 2022, **6**, 280-296.
21. S. Gu, H. Wang, C. Wu, Y. Bai, H. Li and F. Wu, *Energy Storage Materials*, 2017, **6**, 9-17.
22. G. Li, J. Tu, M. Wang and S. Jiao, *Journal of Materials Chemistry A*, 2019, **7**, 8368-8375.
23. Y. Zhang, S. Liu, Y. Ji, J. Ma and H. Yu, *Adv Mater*, 2018, **30**, e1706310.

24. C. Li, X. Zhang and W. He, *Journal of Materials Science: Materials in Electronics*, 2018, **29**, 14353-14370.
25. J. Chen, D. H. C. Chua and P. S. Lee, *Small Methods*, 2019, **4**.
26. T. Mori, Y. Orikasa, K. Nakanishi, C. Kezheng, M. Hattori, T. Ohta and Y. Uchimoto, *Journal of Power Sources*, 2016, **313**, 9-14.
27. Z. Zhao, Z. Hu, R. Jiao, Z. Tang, P. Dong, Y. Li, S. Li and H. Li, *Energy Storage Materials*, 2019, **22**, 228-234.
28. T. Cai, L. Zhao, H. Hu, T. Li, X. Li, S. Guo, Y. Li, Q. Xue, W. Xing, Z. Yan and L. Wang, *Energy & Environmental Science*, 2018, **11**, 2341-2347.
29. H. Hong, J. Liu, H. Huang, C. Atangana Etogo, X. Yang, B. Guan and L. Zhang, *J Am Chem Soc*, 2019, **141**, 14764-14771.
30. L. Yao, S. Ju, T. Xu and X. Yu, *ACS Nano*, 2021, **15**, 13662-13673.
31. Z. Yuan, Q. Lin, Y. Li, W. Han and L. Wang, *Advanced Materials*, 2023, **35**, 2211527.
32. Z. Yu, S. Jiao, J. Tu, Y. Luo, W.-L. Song, H. Jiao, M. Wang, H. Chen and D. J. A. n. Fang, 2020, **14**, 3469-3476.
33. S. Wang, S. Jiao, J. Wang, H. S. Chen, D. Tian, H. Lei and D. N. Fang, *ACS Nano*, 2017, **11**, 469-477.
34. J. Shi, J. Zhang and J. Guo, *ACS Energy Letters*, 2019, **4**, 2124-2129.
35. L. Geng, J. P. Scheifers, C. Fu, J. Zhang, B. P. T. Fokwa and J. Guo, *ACS Appl Mater Interfaces*, 2017, **9**, 21251-21257.
36. M. L. Aubrey and J. R. Long, *J Am Chem Soc*, 2015, **137**, 13594-13602.
37. H. Yang, L. Yin, J. Liang, Z. Sun, Y. Wang, H. Li, K. He, L. Ma, Z. Peng, S. Qiu, C. Sun, H. M. Cheng and F. Li, *Angew Chem Int Ed Engl*, 2018, **57**, 1898-1902.
38. J. Xie and Q. Zhang, *Small*, 2019, **15**, e1805061.
39. Y. Du, B. Zhang, W. Zhang, H. Jin, J. Qin, J. Wan, J. Zhang and G. Chen, *Energy Storage Materials*, 2021, **38**, 231-240.
40. J. Li, W. Luo, Z. Zhang, F. Li, Z. Chao and J. Fan, *Journal of Colloid and Interface Science*, 2023, **639**, 124-132.
41. B. Zhang, R. Kang, W. Zhou, Y. Du, H. Wang, J. Wan and J. Zhang, *ACS Applied Energy Materials*, 2023, **6**, 3366-3373.
42. T. Liu, G. Lv, M. Liu, C. Zhao, L. Liao, H. Liu, J. Shi, J. Zhang and J. Guo, *ACS Applied Materials & Interfaces*, 2023, **15**, 11906-11913.
43. S. Wang, S. Zhao, X. Guo and G. Wang, *Advanced Energy Materials*, 2021, DOI: 10.1002/aenm.202100864.
44. S. Xiao, X. Li, W. Zhang, Y. Xiang, T. Li, X. Niu, J. S. Chen and Q. Yan, *ACS Nano*, 2021, DOI: 10.1021/acsnano.1c03056.
45. Y. Zheng, T. Zhou, C. Zhang, J. Mao, H. Liu and Z. Guo, *Angew Chem Int Ed Engl*, 2016, **55**, 3408-3413.
46. Y. Li, J. Qian, M. Zhang, S. Wang, Z. Wang, M. Li, Y. Bai, Q. An, H. Xu, F. Wu, L. Mai and C. Wu, *Adv Mater*, 2020, **32**, e2005802.
47. X. Ma, J. Chen and W. Zhao, *Nanoscale*, 2020, **12**, 22161-22172.
48. X. Xie, Z. Ao, D. Su, J. Zhang and G. Wang, *Advanced Functional Materials*,

2015, **25**, 1393-1403.
49. S. Huang, Z. Wang, Y. Von Lim, Y. Wang, Y. Li, D. Zhang and H. Y. Yang, *Advanced Energy Materials*, 2021, **11**.
50. N. Zhang, S. Ruan, F. Qu, Y. Yin, X. Li, S. Wen, S. Adimi, J. J. S. Yin and A. B. Chemical, 2019, **298**, 126887.
51. X. Wang, L. Yu, B. Y. Guan, S. Song and X. W. J. A. m. Lou, 2018, **30**, 1801211.
52. J. Yang, Y. Niu, J. Huang, L. Liu and X. J. E. A. Qian, 2020, **330**, 135333.
53. J. Shi, F. Qiu, W. Yuan, M. Guo and Z.-H. J. C. E. J. Lu, 2021, **403**, 126312.
54. Q. Chen, X. Zhang, S. Li, J. Tan, C. Xu and Y. J. C. E. J. Huang, 2020, **395**, 125130.
55. Y. Yin, M. Rioux Robert, K. Erdonmez Can, S. Hughes, A. Somorjai Gabor and A. P. Alivisatos, *Science*, 2004, **304**, 711-714.
56. J. Feng and Y. Yin, *Adv Mater*, 2019, **31**, e1802349.
57. B. D. Anderson and J. B. Tracy, *Nanoscale*, 2014, **6**, 12195-12216.
58. Q. Wei, X. Chang, D. Butts, R. DeBlock, K. Lan, J. Li, D. Chao, D.-L. Peng and B. Dunn, *Nature Communications*, 2023, **14**, 7.
59. L. Zhang, X. Li, L. Tai, C. Shen, J. Yang, C. Sun, H. Geng and X. Zuo, *Nanoscale*, 2021, **13**, 18578-18585.
60. P. Ge, H. Hou, S. Li, L. Yang and X. Ji, *Advanced Functional Materials*, 2018, **28**, 1801765.
61. Q. Mi, D. Zhang, X. Zhang and D. Wang, *Journal of Alloys and Compounds*, 2021, **860**, 158252.
62. S.-S. Mai, K.-Y. Hsiao, Y.-C. Yang, Y.-R. Lu, M.-Y. Lu, Y.-Y. Hsieh, C.-B. Chang and H.-Y. Tuan, *Chemical Engineering Journal*, 2023, **474**, 145992.